

Inboard and outboard radial electric field wells in the H- and I-mode pedestal of Alcator C-Mod and poloidal variations of impurity temperature

C Theiler¹, R M Churchill¹, B Lipschultz², M Landreman³, D R Ernst¹, J W Hughes¹, P J Catto¹, F I Parra⁴, I H Hutchinson¹, M L Reinke¹, A E Hubbard¹, E S Marmor¹, J T Terry¹, J R Walk¹ and the Alcator C-Mod Team

¹ Plasma Science and Fusion Center, Massachusetts Institute of Technology (MIT), Cambridge, MA 02139

² York Plasma Institute, University of York, Heslington, York, YO10 5DD

³ Institute for Research in Electronics and Applied Physics, University of Maryland, College Park, MD 20742

⁴ Rudolf Peierls Centre for Theoretical Physics, University of Oxford, Oxford, UK

Abstract. We present inboard (HFS) and outboard (LFS) radial electric field (E_r) and impurity temperature (T_z) measurements in the I-mode and H-mode pedestal of Alcator C-Mod. These measurements reveal strong E_r wells at the HFS and the LFS midplane in both regimes and clear pedestals in T_z , which are of similar shape and height for the HFS and LFS. While the H-mode E_r well has a radially symmetric structure, the E_r well in I-mode is asymmetric, with a stronger ExB shear layer at the outer edge of the E_r well, near the separatrix. Comparison of HFS and LFS profiles indicates that impurity temperature and plasma potential are not simultaneously flux functions. Uncertainties in radial alignment after mapping HFS measurements along flux surfaces to the LFS do not, however, allow direct determination as to which quantity varies poloidally and to what extent. Radially aligning HFS and LFS measurements based on the T_z profiles would result in substantial inboard-outboard variations of plasma potential and electron density. Aligning HFS and LFS E_r wells instead also approximately aligns the impurity poloidal flow profiles, while resulting in a LFS impurity temperature exceeding the HFS values in the region of steepest gradients by up to 70%. Considerations based on a simplified form of total parallel momentum balance and estimates of parallel and perpendicular heat transport time scales seem to favor an approximate alignment of the E_r wells and a substantial poloidal asymmetry in impurity temperature.

1. Introduction

The physics processes in the edge region of magnetically confined fusion plasmas are of primary importance, determining the level of particle and heat transport into the unconfined, open field line region and serving as boundary condition for the core plasma. At the transition from low-confinement (L-mode) to high-confinement (H-mode) [1] regimes, an edge transport barrier (ETB) forms. The ETB is located just inside the last closed flux surface and its width corresponds to a few percent of the plasma radius [2, 3]. Turbulence is strongly suppressed in the ETB and temperature and density develop strong gradients, referred to as a *pedestal*. Due to profile stiffness, pedestal formation results in a strong increase of total stored energy in the plasma, leading to a substantial boost of energy confinement and fusion performance [4]. Besides standard H-modes that are usually subject to intermittent bursts called edge-localized modes (ELMs) of concern for future fusion reactors [5], there has been a relatively recent focus on ETBs without ELMs, such as in I-mode [6], EDA H-mode [7], and QH-mode [8]. It is now widely accepted that turbulence suppression and reduction of heat transport in ETBs is caused by a strongly sheared radial electric field E_r and the associated sheared ExB flow [9, 10]. Despite substantial progress, a first principles understanding of ETBs has not yet been obtained. Numerical and analytical studies are complicated by the short radial scale lengths in the pedestal [11, 12] and experimental measurements are challenging and usually limited to a single poloidal location, such that information about variations of plasma parameters on a flux surface is often missing. As poloidal asymmetries are expected to scale with the ratio of poloidal Larmor radius and radial scale length [13], they could be important in the pedestal region. Recent neoclassical calculations have indeed revealed strong poloidal asymmetries associated with steep pedestal gradients [12, 14].

In this paper, we present new experimental insights on the poloidal structure of the pedestal. In particular, our measurements indicate that in the pedestal, plasma potential and temperature are not necessarily constant on a flux surface. The measurements, performed on the Alcator C-Mod tokamak [15, 16, 17], are enabled using a recently developed gas-puff charge exchange recombination spectroscopy technique (GP-CXRS) [18], allowing for measurements at both the inboard or high-field side (HFS) and the outboard or low-field side (LFS) midplane. This technique has previously allowed insights about poloidal variations of toroidal flow and impurity density on Alcator C-Mod [19, 20] and ASDEX-U [21, 22]. As shown here, GP-CXRS reveals clear E_r wells and impurity temperature pedestals at both measurement locations in I-mode and EDA H-mode plasmas. When HFS measurements are mapped along magnetic flux surfaces to the LFS, there is an uncertainty in the radial alignment of HFS and LFS profiles due to uncertainties in the magnetic reconstruction. Aligning the profiles such that the impurity temperature profiles align results in an outward shift of the HFS E_r well with respect to the LFS one by a substantial fraction of its width. On the other hand, aligning the location of the E_r wells results in LFS to HFS impurity temperature ratios

up to ≈ 1.7 .

In Sec. 2, we discuss the experimental setup and diagnostic technique. Radial electric field measurements are presented in Sec. 3, followed by inboard-outboard comparisons in Sec. 4. In the latter, we also discuss questions related with the measurement technique and give further details in Appendix A. Sec. 5 describes simplified estimates to determine which species are expected to have poloidally varying temperature, what poloidal potential asymmetries imply for the electron density, and what insights we get from total parallel force balance. Sec. 6 summarizes the results.

2. Experimental setup and diagnostics

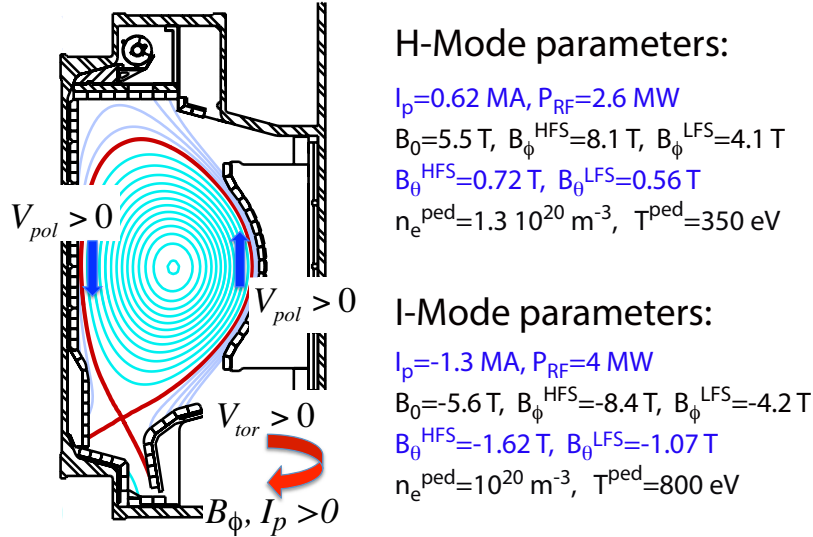


Figure 1. Left: Typical magnetic equilibrium of a lower single null discharge on C-Mod. Arrows indicate the positive direction of HFS and LFS poloidal flows as well as toroidal flow, magnetic field, and plasma current. Right: Some key parameters of the discharges discussed in this paper.

The experiments are performed on the Alcator C-Mod tokamak at MIT, a compact, all-metal walled device operating at magnetic fields, densities, neutral opacity, and parallel heat fluxes similar to those expected in ITER. Here, we focus on measurements in enhanced D-alpha (EDA) H-mode [7] and I-mode [23, 24, 6, 25, 26]. These are both high-confinement regimes with an ETB that typically does not feature ELMs. Different edge instabilities, the quasi-coherent mode in EDA H-mode [7] and the weakly coherent mode in I-mode [6, 27, 28], are believed to regulate particle transport and avoid impurity accumulation in these regimes. EDA H-modes are obtained at high collisionality, while I-mode is a low collisionality regime, usually obtained with the ion ∇B drift away from the active X-point. The decoupling between energy and particle transport in I-mode, as well as other properties [6, 25, 29], make it a promising regime for future fusion reactors. Some key scalar parameters of the EDA H-mode and I-mode discharge investigated here

are given in Fig. 1. Both discharges are run in a lower single null configuration. The I-mode discharge is performed in reversed field, with toroidal field and plasma current in the counter-clockwise direction if viewed from above. Fig. 2 displays radial profiles at the LFS midplane of the ion Larmor radius ρ_i and $\rho_i^\theta = \frac{B}{B_\theta} \rho_i$, the radial temperature and electron density scale lengths $L_T = |T_z/(dT_z/dr)|$ and $L_{ne} = |n_e/(dn_e/dr)|$, and the collisionality [30] $\nu^* = \hat{\nu}_{ii}qR/(\epsilon^{1.5}v_{th,i})$ in these plasmas. Electron density n_e is measured at the top of the machine with the Thomson scattering diagnostic [31] and mapped along magnetic flux surfaces to the LFS midplane. In Fig. 2, we also show the radial profile of the impurity (B^{5+}) temperature, T_z , revealing a clear pedestal. Here and throughout this paper, the radial coordinate $\rho = r/a_0$ is used. It is a flux surface label, where r is the radial distance of a flux surface at the LFS midplane from the magnetic axis and a_0 is the value of r for the last closed flux surface (LCFS). Typically, $a_0 \approx 22$ cm on C-Mod. Fig. 2 shows that for the H-mode case, the main ions are in the plateau regime, $1 < \nu^* < \epsilon^{-1.5} \approx 6$, and, from the center of the T_z pedestal at $\rho \approx 0.985$ outwards (towards larger minor radii), in the Pfirsch-Schlüter regime. In I-mode, main ions are in the banana regime, $\nu^* < 1$, almost all the way to the LCFS. In agreement with previous studies [3, 6], we find that in the pedestal region both L_T and L_{ne} can be comparable to ρ_i^θ . These are conditions not covered by any current analytical treatment of neoclassical theory (see e.g. [12]). We note that depending on the application, a more accurate expression for ν^* than the one above could be used [32, 33]. Replacing q by $L_{||}/(\pi R)$ for instance, with $L_{||}$ the distance along the magnetic field between LFS and HFS midplane when going around the direction opposite to the X-point, would reduce ν^* near the separatrix, by a factor 0.65-0.75 for $\rho=0.99-0.999$.

The main diagnostic used in this work is GP-CXRS [18]. A localized source of neutrals leads to charge exchange reactions with fully stripped impurities, with the exchanged electron usually transitioning into an excited state of the impurity. Collecting and analyzing the line radiation emitted after de-excitation of the impurity excited state thus provides localized measurements of impurity temperature, flow, and density. In contrast to traditional CXRS [34, 35, 36], which uses a high energy neutral beam as a neutral source to locally induce charge exchange reactions, GP-CXRS uses a thermal gas puff instead. Even though the density of neutrals injected by the gas puff decreases strongly as a function of distance into the plasma, this technique allows for excellent light levels across the entire pedestal region at Alcator C-Mod. Furthermore, gas puffs can be installed all around the periphery of the tokamak, allowing for measurements at different poloidal locations.

Since the 2012 experimental campaign on C-Mod, a complete GP-CXRS system with poloidal and toroidal optics at both the HFS and LFS midplane is operational [18]. These systems provide the necessary measurements to deduce the radial electric field from the radial impurity force balance:

$$E_r = \frac{1}{n_z Z e} \frac{d(n_z T_z)}{dr} - V_{z,\theta} B_\phi + V_{z,\phi} B_\theta. \quad (1)$$

Here, n_z represents the impurity density, in this case that of fully stripped boron (B^{5+}).

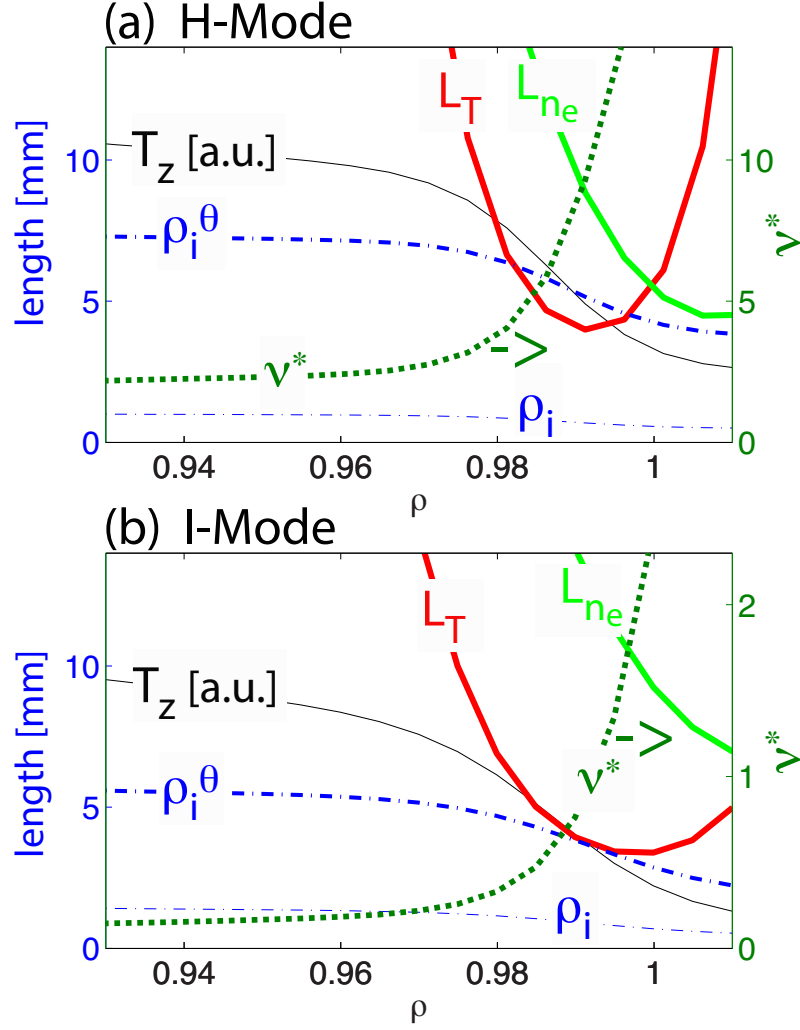


Figure 2. Radial profiles at the LFS midplane of some key parameters of the H-mode (a) and I-mode (b) discharge discussed in this work: main ion Larmor radius (total and poloidal), radial temperature and electron density scale length, and (main ion) collisionality. The latter is plotted on the right axis. For reference, the LFS boron temperature profile T_z is also shown.

Z is the charge state (here $Z = 5$), T_z the temperature, $V_{z,\theta}$ and $V_{z,\phi}$ the poloidal and toroidal velocity, B_θ and B_ϕ the poloidal and toroidal component of the magnetic field, and e the unit charge. Regardless of the direction of the magnetic field or the plasma current, toroidal components of magnetic field and velocity are defined as positive if they point along the clockwise direction if viewed from above. Poloidal field and velocity components are defined positive when upwards at the LFS and downwards at the HFS. This convention is illustrated in Fig. 1. HFS and LFS magnetic field components representative of the pedestal region of the plasmas investigated here are listed in Fig. 1.

3. HFS and LFS profiles of E_r and T_z

Fig. 3 (a) shows LFS GP-CXRS measurements for the EDA H-mode, with edge radial profiles of parallel and perpendicular impurity temperature in the top panel and the radial electric field together with the contribution from the individual terms in Eq. (1) in the bottom panel. A temperature pedestal with good agreement between perpendicular and parallel temperatures is apparent. In the pedestal region, a clear E_r well is present. The main contribution in Eq. (1) to the structure of the E_r well comes from the impurity poloidal velocity and diamagnetic term. This agrees with earlier measurements from beam based CXRS on C-Mod [24], although GP-CXRS measurements seem to give somewhat stronger contributions from the diamagnetic term. The toroidal velocity is co-current and mainly contributes a constant offset. A local minimum in toroidal velocity as reported from other tokamaks [37] is often observed but relatively weak in the present case.

Fig. 3 (b) shows the equivalent measurements for the HFS. The same flux surface label

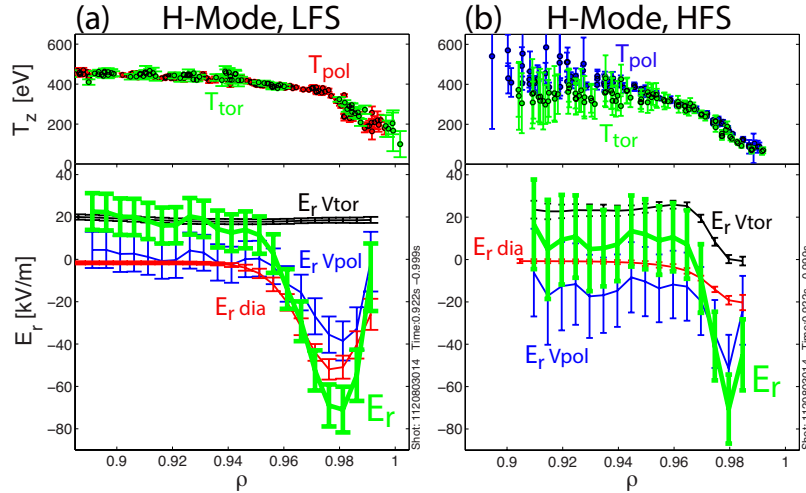


Figure 3. (a): GP-CXRS measurements (B^{5+}) at the LFS midplane in H-mode. The top panel shows boron temperatures measured with poloidal and toroidal viewing optics. The bottom panel shows the radial electric field obtained using Eq. (1). $E_{r,dia}$, $E_{r,Vpol}$, and $E_{r,Vtor}$ show, respectively, the contributions from the individual terms on the right of Eq. (1). (b): the same as in (a) for measurements at the HFS midplane.

ρ is used as the radial coordinate. An E_r well is measured in the pedestal region, similarly to the LFS. However, the different terms in Eq. (1) contribute in a different way. As reported earlier [19], at the HFS, the toroidal velocity is co-current at the pedestal top and strongly decreases towards the LCFS. Therefore, besides the poloidal velocity term, the toroidal velocity term contributes also significantly to the shape of the E_r well. Another difference compared to the LFS is that the impurity diamagnetic term contributes less to the E_r well. The reason for this becomes clear when we write this term as $\frac{1}{Ze} \frac{dT_z}{dr} + \frac{T_z}{Zen_z} \frac{dn_z}{dr}$. The flux surface spacing is larger at the HFS than it is on the LFS, by typically about 40%. Therefore, the magnitude of radial gradients of flux func-

tions is smaller. Secondly, and this is more important here, the HFS impurity density profile is shifted outwards compared to the temperature profile, while the opposite is true on the LFS [20]. Therefore, for the HFS, the term proportional to the logarithmic derivative of density gets multiplied with a smaller temperature value T_z than for the LFS. Finally, we note that assuming that plasma potential is a flux function, we expect that the E_r well is deeper on the LFS than it is on the HFS: $E_r = -\frac{d\Phi}{dr} = -\frac{d\Phi}{d\rho} \cdot \frac{d\rho}{dr}$, and $|\frac{d\rho}{dr}| \approx 5 \text{ m}^{-1}$ on the LFS and $|\frac{d\rho}{dr}| \approx 3.6 \text{ m}^{-1}$ on the HFS. Within error bars, measurements are marginally consistent with these values.

Fig. 4 shows LFS and HFS GP-CXRS measurements in I-mode. A clear E_r well is apparent, comparable in depth to the EDA H-mode case and only slightly wider than the full width at half maximum of $\approx 4 \text{ mm}$ in H-mode. Due to the excellent light levels of GP-CXRS across the pedestal, the LFS E_r profile shows details that have not been observed previously on C-Mod. The poloidal velocity is mostly along the electron diamagnetic drift direction. It shows only a weak dip around the mid-pedestal, where a strong dip is observed in H-mode. At somewhat larger minor radii, however, there is a strong shear in poloidal velocity and the velocity is oriented along the ion-diamagnetic drift direction near the LCFS. While diamagnetic and toroidal velocity terms also contribute to the structure of E_r , this shear in poloidal velocity is responsible for an asymmetric E_r well in I-mode, with a stronger shear layer at the outer edge of the E_r well. This asymmetric structure is actually observed in all I-modes investigated with GP-CXRS. HFS measurements in I-mode also reveal an E_r well. It is determined mainly by the poloidal and the toroidal velocity terms in Eq. (1). As in H-mode, toroidal velocity is also co-current in I-mode [38] and strongly sheared near the LCFS at the HFS.

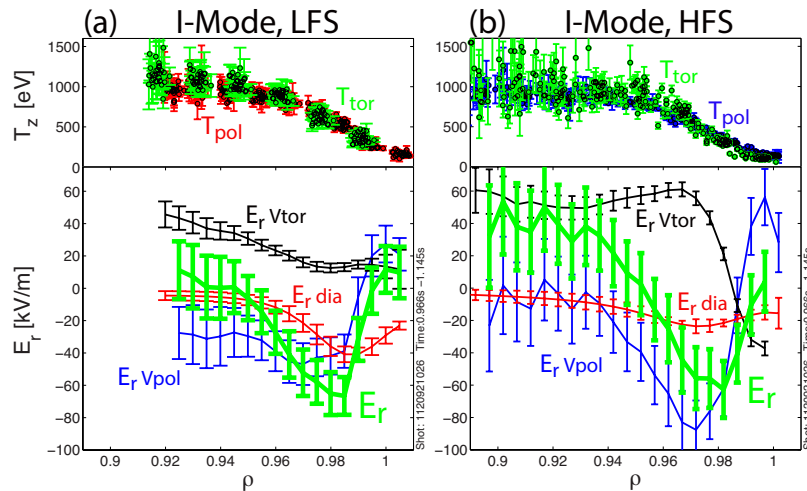


Figure 4. The equivalent to Fig. 3 for I-mode.

4. Poloidal variations of temperature and potential

In Figs. 3 and 4, we have shown HFS and LFS radial profiles of T_z and E_r as a function of the coordinate ρ . For the mapping of the discrete radial measurement locations of the CXRS diagnostics to ρ -space, we have used magnetic equilibrium reconstruction from normal EFIT [39]. Due to uncertainties in the reconstructed location of the LCFS of $\approx 5\text{mm}$ [40, 20], there is some freedom in the radial alignment of HFS and LFS profiles. Throughout this paper, for LFS data, the location of the LCFS, $\rho = 1$, is adjusted such that it approximately coincides with the temperature pedestal foot location. This requires radial shifts of $\Delta\rho = 0.01$ (H-mode) and $\Delta\rho = 0.03$ (I-mode) with respect to the position indicated by EFIT. We now discuss different approaches to align HFS data with respect to LFS data.

For the study of poloidal variations of impurity density [20] and toroidal flow [19] on C-Mod, impurity temperature was assumed to be a flux function and HFS and LFS profiles have been aligned to best satisfy this assumption. This is the alignment adopted in Figs. 5 (a) and 6 (a). The top panels in Figs. 5 (a) and 6 (a) show the radially aligned HFS and LFS poloidal temperatures and the bottom panels show the corresponding E_r profiles. It is apparent that this alignment results in a significant radial shift between the HFS and LFS E_r wells, with the HFS well shifted outwards with respect to the LFS one. The shift is about $\Delta\rho = 0.015$ in the H-mode case, which corresponds to $\approx 3\text{ mm}$. In the I-mode case, the shift is about $\Delta\rho = 0.012$, corresponding to $\approx 2.5\text{ mm}$. Even though these shifts are relatively small, they can not be explained by uncertainties in the reconstructed location of the LCFS. There is no freedom in aligning the *individual* quantities measured with CXRS at either the LFS or the HFS, such as for example the LFS impurity temperature and E_r . An exception is when instrumental effects become important, which is discussed below.

Instead of aligning the temperature profiles, in Figs. 5 (b) and 6 (b), we have aligned HFS and LFS profiles such that the location of the E_r wells align. This alignment of course now results in substantial differences between HFS and LFS impurity temperatures in the pedestal region, with LFS values exceeding the HFS ones by a factor of up to ≈ 1.7 .

We note that we used an alignment of the E_r wells in Figs. 5 (b) and 6 (b) as a proxy to minimize the HFS - LFS asymmetry in plasma potential Φ . Indeed, assuming plasma potential is a flux function, we can determine the expected HFS E_r profile from the LFS one as follows

$$E_r^{HFS}(\rho) = \left(\frac{d\rho}{dr}\right)_{HFS} \cdot \left(\frac{dr}{d\rho}\right)_{LFS} \cdot E_r^{LFS}(\rho). \quad (2)$$

At the LFS midplane, $d\rho/dr$ is constant. For the HFS midplane, magnetic reconstruction shows that $d\rho/dr$ radially varies by $\lesssim 7\%$ across the pedestal region. Therefore, if plasma potential is a flux function, within a good approximation, HFS and LFS E_r wells differ by a constant factor only and in particular the E_r wells radially align. In Figs. 5 (b) and 6 (b), we show the HFS E_r profile calculated from Eq. (2) as a red curve. For

better visibility, error bars have been omitted. They are dominated by the error bars of E_r^{LFS} . In the I-mode case, Fig. 6 (b), aligning estimated and measured HFS E_r wells is straightforward. In the H-mode case, Fig. 5 (b), the measured HFS E_r well is somewhat narrower than expected from the LFS measurement and the assumption that Φ is a flux function. There is thus some ambiguity on how to align the profiles. One could argue that measured and estimated HFS E_r profiles should rather match across the inside edge of the well. In this case, the radial shift between HFS and LFS T_z profiles would rather be $\Delta\rho = 0.02$ instead of $\Delta\rho = 0.015$, which would not qualitatively change our conclusions. In principle, a more accurate approach would be to directly align the plasma potential profiles in Figs. 5 (b) and 6 (b). We use here the E_r wells because E_r is experimentally the more readily inferred quantity and any systematic errors in E_r accumulate if E_r is radially integrated.

It is interesting to note that when E_r wells are aligned, HFS and LFS poloidal impurity flow profiles also approximately align. In the I-mode case, HFS and LFS poloidal flows are then actually identical within error bars and in particular the change from electron to ion diamagnetic flow direction occurs at the same radial location. The latter is consistent with the expression of the poloidal flow, $V_\theta(\rho, \theta) = K_z(\rho)B_\theta(\rho, \theta)/n_z(\rho, \theta)$ with $K_z(\rho)$ a flux function [19], valid if sources/sinks and the divergence of the radial impurity flux are negligible. Indeed, independent of poloidal asymmetries in impurity density [20], we would then expect the zero crossing of V_θ to occur at the same ρ anywhere on a flux surface. In the H-mode case, the magnitude of the poloidal flow peaks differ for HFS and LFS measurements, but their radial locations also approximately match when E_r wells are aligned. These observations can be inferred from the poloidal velocity contribution to E_r in Figs. 3 and 4 (in these plots, HFS and LFS data have been aligned based on the location of the E_r well). These observations seem to speak in favor of the alignment in Figs. 5 (b) and 6 (b). However, we should note that from recent theoretical calculations[12], we do not necessary expect the HFS and LFS poloidal flow structures to align.

The first question that arises is whether these unexpected shifts between HFS and LFS E_r well and/or impurity temperature profiles can be explained by measurements issues. Therefore, we have studied the GP-CXRS techniques and its subtleties in detail [18]. This shows that cross-section effects can lead to an overestimation of the impurity temperature in regions where the temperature of the neutrals resulting from the gas puff is much lower than the impurity temperature. Simulations of gas puff penetration show, however, that in the pedestal region, the neutral temperature is at least 30% of the ion temperature and in this case, cross-section effects lead to an overestimation of the impurity temperature of not more than 15%. In addition, cross-section effects should affect LFS and HFS measurements similarly. Another potential concern is the contamination of the spectrum by molecular emission from the gas puff. This effect is important mainly in the region from the LCFS on outwards and, if not accounted for, results in rising temperatures in the SOL. In [18], we have presented a heuristic

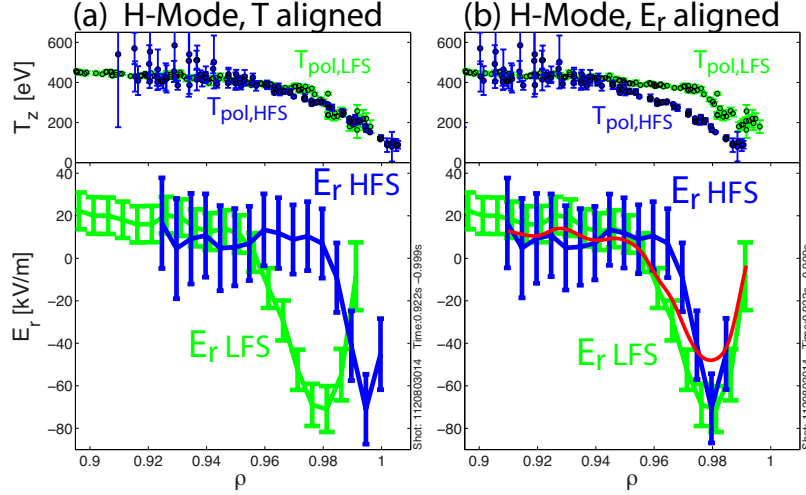


Figure 5. Effects of different radial alignments of the HFS and LFS measurements for the H-mode of Fig. 3. In (a), profiles are aligned such that the T_z profiles align. In (b), the E_r wells are aligned instead. Also shown in (b) as a red curve is the HFS E_r well calculated from Eq. (2). It is the HFS E_r profile expected from the LFS measurement and the assumption that plasma potential is a flux function.

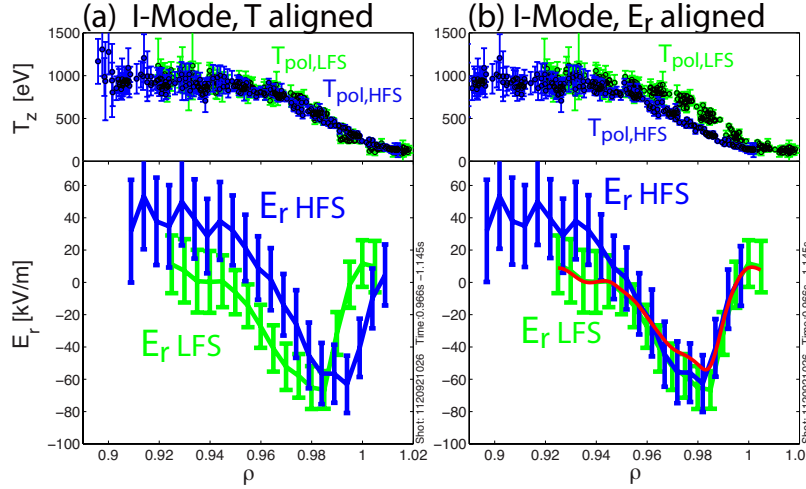


Figure 6. The equivalent to Fig. 5 for I-mode.

approach to correct for these effects. This approach was validated in a number of I-mode plasmas using alternatively deuterium gas puffs and helium gas puffs. Another potential measurement issue are instrumental effects associated with flux surface curvature and finite chord width, which could cause smoothing of profiles as well as shifts between the different quantities. Ongoing studies based on a synthetic diagnostic show that these effects are weak in the discharges discussed here.

Finally, there is the question whether the gas puff perturbs the plasma being measured, either locally or globally. In Appendix A, we present a theoretical estimate, which indicates that cooling of the main ions (or the impurities) by the gas puff is not strong enough to cause a substantial local decrease in ion temperature. Also, using

experimental data, we show that at the LFS where puff rates change relatively quickly over time, the measured plasma parameters typically do not depend on the instantaneous puff rate. While fully understanding the local and global effects of gas puffs on the plasma is challenging (see [41] and references therein), the studies in Appendix A suggest that gas puff perturbation is not responsible for the observed poloidal asymmetries. In the next section, we explore physics explanations for the observed misalignments between HFS and LFS profiles.

5. Simplified theoretical considerations

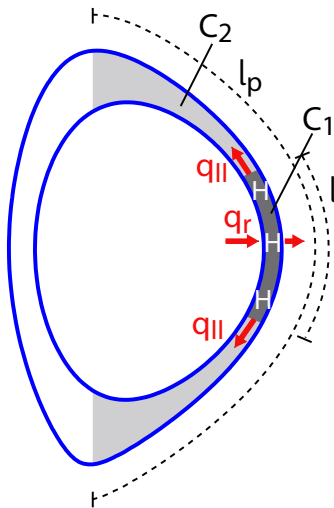


Figure 7. Poloidal sketch of the volume between two nearby flux surfaces. A heat source H , extending poloidally over a distance l , defines control volume C_1 . The origin of H is e.g. the divergence of the radial heat flux. The heat source is balanced by parallel heat conduction. The larger volume C_2 , with poloidal extent l_p , represents an estimate of the average volume accessible to a trapped particle.

Based on simplified model equations, we investigate now the possibility of poloidal variations of electron, ion, and impurity temperature. We then also discuss the implications of different shifts between HFS and LFS E_r wells on the poloidal variations of electron density and how our measurements agree with total parallel momentum balance.

We start with a time scale analysis to see if a poloidally localized heat source in the pedestal, e.g. due to ballooning transport, can generate a poloidal asymmetry in T_e , T_i , or T_z , or if parallel heat transport is sufficiently strong to ensure poloidal symmetry of these quantities. We consider the energy conservation equation in the following form

$$\frac{3}{2}n_a \left(\frac{\partial}{\partial t} + \mathbf{V}_a \cdot \nabla \right) T_a + p_a \nabla \cdot \mathbf{V}_a = -\nabla \cdot \mathbf{q}_a - \boldsymbol{\pi}_a : \nabla \mathbf{V}_a + Q_a. \quad (3)$$

The subscript a stands for the species of interest and \mathbf{q}_a , $\boldsymbol{\pi}_a$, and Q_a are the conductive heat flux, the viscosity tensor, and the energy exchange between species, respectively

(see e.g. [30]). To evaluate the time scales associated with the different terms in Eq. (3), we assume a situation as sketched in Fig. 7. A poloidally localized heat source H extends over a poloidal distance l . Together with two nearby flux surfaces shown in blue in Fig. 7, this defines a control volume C_1 . We assume that the heat source H causes an inboard-outboard temperature asymmetry of order one and that n_a and T_a are approximately constant inside C_1 . Parallel heat conduction then acts to reduce this inboard-outboard temperature asymmetry on a time scale τ_a^{\parallel} defined by $\nabla \cdot \mathbf{q}_{a\parallel} \approx \frac{3}{2}n_a T_a (\tau_a^{\parallel})^{-1}$. We now estimate τ_a^{\parallel} and determine whether any term in Eq. (3) can drive temperature asymmetries on a comparable time scale. If not, we discard the possibility of significant poloidal variations of T_a .

We integrate Eq. (3) over the volume C_1 and for a given term A of the integrated Eq. (3), we define the associated time scale τ^A as

$$\tau^A \approx \frac{3}{2}n_a T_a C_1 / A. \quad (4)$$

For the integration of $\nabla \cdot \mathbf{q}_{a\parallel}$, using the divergence theorem, we then find

$$\tau_a^{\parallel} = \frac{3n_a T_a l}{4q_{a\parallel} \frac{B_{\theta}}{B}}. \quad (5)$$

We first consider the case of high collisionality, $v_{th,a}/\nu_a \ll L_{\parallel}$, where $v_{th,a} = \sqrt{2T_a/m_a}$ is the thermal velocity of species a , ν_a its collision frequency, and L_{\parallel} the distance along the magnetic field between the inboard and outboard side. We take the Braginskii expression[30] for parallel heat conduction, $\mathbf{q}_{a\parallel}^{Brag} = -\kappa_{\parallel,a} \nabla_{\parallel} T_a$, where $\kappa_{\parallel,a} \approx 3n_a T_a \tau_a / m_a$, i.e. we approximate the numerical factor (3.9 for ions and 3.16 for the electrons[30]) by 3. Inserting this expression into Eq. (5) and setting $\nabla_{\parallel} T_a \approx T_a / L_{\parallel}$, we get

$$\tau_a^{\parallel, Brag} \approx \frac{1}{2} \frac{L_{\parallel} l \frac{B}{B_{\theta}}}{v_{th,a}^2} \nu_a. \quad (6)$$

At low collisionality, on the other hand, the free streaming expression, $q_{a\parallel}^{fs} \approx \frac{3}{2}n_a T_a v_{th,a}$ is more appropriate. This results in a time scale

$$\tau_a^{\parallel, fs} \approx \frac{1}{2} \frac{l \frac{B}{B_{\theta}}}{v_{th,a}}. \quad (7)$$

To interpolate $q_{a\parallel}$ between these two limits, similarly to Ref. [42] and references therein, we perform a harmonic average such that $q_{a\parallel} = (1/q_{a\parallel}^{Brag} + 1/q_{a\parallel}^{fs})^{-1}$. This is equivalent to adding up the corresponding time scales and we define

$$\tau_a^{\parallel, low} \approx \tau_a^{\parallel, Brag} + \tau_a^{\parallel, fs} \approx \frac{1}{2} \frac{l \frac{B}{B_{\theta}}}{v_{th,a}} \left(\frac{L_{\parallel}}{v_{th,a}} \nu_a + 1 \right). \quad (8)$$

For our estimate of $\tau_a^{\parallel, low}$, we neglected the fact that at low collisionality, a large fraction of particles at the LFS are magnetically trapped. As can be inferred from Eq. (25) in [43], $\tau_a^{\parallel, low}$ therefore underestimates the time scale τ_a^{\parallel} .

We now heuristically evaluate an upper bound for τ_a^{\parallel} , labelled $\tau_a^{\parallel, up}$, which accounts for

trapped particles. We assume that particles which are heated up in volume C_1 or high energy particles entering C_1 by cross-field transport, are all trapped at low collisionality, such that they do not reach the HFS on the free streaming time scale $L_{\parallel}/v_{th,a}$. Instead, they are confined to a volume which depends on their pitch angle. For simplicity, we assume that trapped particles are on average confined to the volume C_2 indicated in Fig. 7. The important point here is that C_2 constitutes a substantial fraction of the total volume defined by the two flux surfaces, while, depending on the heat source, C_1 can be much smaller. The trapped particles get detrapped at a frequency ν_a/ϵ , where ϵ is the inverse aspect ratio. The number of particles that get detrapped per unit time in the volume C_2 is given by $C_2 n_a \nu_a / \epsilon$, each transporting on average an energy $\frac{3}{2} T_a$ to the HFS. As all the heat source inside C_2 is contained in C_1 , the resulting power out of C_2 is the same as that out of C_1 . From these considerations, we find a parallel heat flux exiting volume C_1 which is given by $q_{a\parallel}^{tr} \approx \frac{3}{4} T_a n_a \frac{\nu_a}{\epsilon} \frac{B}{B\theta} l_p$, where l_p is the poloidal extent of volume C_2 , Fig. 7. We perform a harmonic average between $q_{a\parallel}^{tr}$ and the parallel heat flux obtained above in absence of particle trapping. Using Eq. (5), we find

$$\tau_a^{\parallel,up} \approx \tau_a^{\parallel,low} + \epsilon \frac{l}{l_p} \frac{1}{\nu_a}. \quad (9)$$

We now estimate the importance of different heat sources which could drive temperature asymmetries and consider first the electrons. The most obvious term in Eq. (3) which can drive temperature asymmetries is the divergence of the radial heat flux $q_{e,r}$. Due to the ballooning nature of turbulent transport, we expect $q_{e,r}$ and its divergence to peak at the LFS. Defining an anomalous heat diffusivity χ_e such that $q_{e,r} = -\frac{3}{2} n_e \chi_e \partial_r T_e$, the time scale associated with heating due to radial heat transport, τ_e^x , is given by

$$\tau_e^x \approx \frac{L_T^2}{\chi_e}, \quad (10)$$

with L_T as before the radial temperature scale length. In order to estimate χ_e , we consider the experimentally measured power P_{sep} crossing the separatrix. We assume that cross-field energy transport occurs primarily at the LFS, across a surface $A_{sep}^{LFS} \approx 2\pi(R_0 + a_0)l$. Setting $l = 2a_0$, A_{sep}^{LFS} corresponds to about 30% of the area of the LCFS. We assume that half of the energy is transported by the electrons and thus set $q_{e,r} = -\frac{3}{2} n_e \chi_e \partial_r T_e \approx P_{sep}/(2A_{sep})$. From this estimate, we deduce profiles of χ_e , which we plug into Eq. (10). We find values of $\chi_e \approx 0.2$ m²/s and $\chi_e \approx 0.35$ m²/s for the H-mode and the I-mode case in the region of steepest temperature gradient and larger values elsewhere.

In Fig. 8, we show τ_e^{\parallel} and τ_e^x across the pedestal region of the H-mode and I-mode case discussed in the previous sections. τ_e^{\parallel} is plotted as a shaded, red area, limited below and above by the expression in Eqs. (8) and (9). We have set $l = 2a_0$ and note that in our model, the ratio of τ_e^{\parallel} and τ_e^x does not depend on the choice of l . It is apparent from Fig. 8 that τ_e^{\parallel} is much lower than τ_e^x over the entire pedestal, suggesting that the drive for electron temperature asymmetries is small compared to the fast temperature equilibration along the magnetic field. Therefore, we expect T_e to be a flux function

across the pedestal region.

The conclusion that T_e should be a flux function in the pedestal region does not change if we consider additional time scales in Eq. (3). The time scale associated with the diamagnetic heat flux [30] is estimated to be $\tau^\wedge \approx \frac{L_T}{\rho_e} \frac{\pi a_0}{v_{th,e}}$ and is shown as a thin, dotted curve in Fig. 8. This term can usually drive up-down asymmetries [30] and we therefore do not expect it to drive in-out asymmetries. However, even if it did, it can not compete with τ_e^\parallel . We next discuss the convective terms on the left of Eq. (3). In the above evaluation of P_{sep} , we have not made a distinction between convective and conductive contributions, so that convective radial heat transport is already included in τ_e^χ . The time scale for convective poloidal heat transport for electrons is found to be comparable to τ^\wedge (not shown), again substantially slower than parallel electron temperature equilibration. Finally, ion-electron temperature equilibration in the pedestal is relatively slow and comparable to τ_e^χ only at the pedestal top (not shown). Therefore, even if T_i varies poloidally, ion-electron heat transfer would not cause asymmetries in T_e .

For the main ions, the time scale τ_i^\parallel is larger than τ_e^\parallel by a factor $\approx \sqrt{m_i/m_e}$ (assuming $T_i \approx T_e$ and $n_i \approx n_e$). This quantity is shown in Fig. 8 by the green, shaded region, again defined by the lower and upper bounds in Eqs. (8) and (9). At the same time, we expect that the time scale for driving ion temperature asymmetries by ballooning transport, τ_i^χ , is similar to τ_e^χ . This is based on the radial scale lengths being similar for ion and electron temperatures in the C-Mod pedestal [19] and the assumption that radial heat flux is carried in approximately equal parts by the ions and the electrons. The latter is consistent with findings from DIII-D[44], where a ratio of electron to ion heat flux of ≈ 2 was found in the pedestal. We note that the transport barrier minima we then find for χ_i (≈ 0.35 m²/s in I-mode and ≈ 0.2 m²/s in EDA H-mode) are consistent with the values of $\approx 0.1 - 0.15$ m²/s reported in the literature [44, 45], considering that the latter are the flux-surface averaged quantities, while we have assumed a χ_i which is non-zero only over $\approx 30\%$ of the flux surface. Clearly, lower values of χ_i or weaker poloidal variations in χ_i than assumed here would reduce the possibility of poloidal T_i variations.

With these estimates, Fig. 8 shows that τ_i^χ can compete with τ_i^\parallel near the separatrix. We should note here that τ_i^\parallel is derived for temperature asymmetries of order 1 and a ratio of $\tau_i^\parallel/\tau_i^\chi \approx 0.2$ would still allow for a 20% poloidal variation of T_i . Furthermore, the free streaming heat flux $q_{i\parallel}^{fs} \approx n_i T_i v_{th,i}$ is often adjusted by a factor of ≈ 0.2 [42], which would bring τ_i^\parallel up even further. Considering this and the approximate nature of these estimates, poloidal variations of T_i , driven by ballooning transport, seem possible, at least across the steep gradient region of the LFS T_z profile, i.e., for $\rho \gtrsim 0.98$ (H-mode) and $\rho \gtrsim 0.97$ (I-mode).

The diamagnetic heat flux time scale τ^\wedge , already discussed for electrons, is similar for ions and electrons. It constitutes an additional drive term for asymmetries, although these are expected to be up-down asymmetries and τ^\wedge is given here merely for completeness.

Finally, we display in Fig. 8 the time scale τ_{zi}^{eq} for thermalization of the impurities (B^{5+})

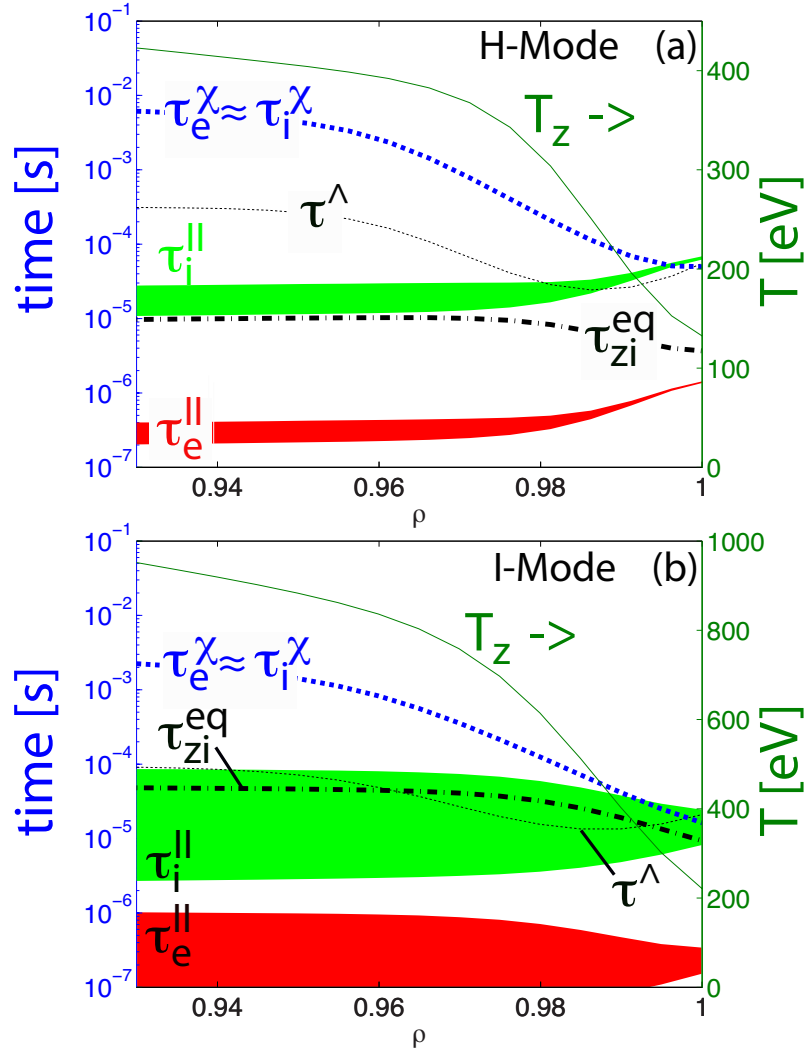


Figure 8. Estimates of heat transport time scales in the H-mode (a) and I-mode (b) discharges discussed here. τ_e^{\parallel} and τ_i^{\parallel} , plotted here as a shaded region bounded by Eqs. (8) and (9), are the time scales for electron and ion temperature to become uniform along the magnetic field, $\tau_e^x \approx \tau_i^x$ is the time scale of heat input due to radial heat transport, τ^{\wedge} the time scale associated with the diamagnetic heat flux, and τ_{zi}^{eq} the time scale for thermalization of the impurities B^{5+} with the main ions. For reference, the LFS boron temperature profile T_z is also shown.

with the main ions (dash-dotted curve). It is calculated assuming an order one temperature difference between the two species, such that e.g. a 20% difference instead would bring this curve up by a factor 5. As the concentration of B^{5+} is relatively low ($\lesssim 2\%$), the radial heat flux time scale τ_z^x could be faster than τ_i^x without violating energy balance. For the H-mode case, τ_z^x would indeed have to be faster than τ_i^x to allow T_z to differ from T_i . For I-mode and $\rho \gtrsim 0.97$, main ion and impurity temperature differences seem possible even for $\tau_z^x \approx \tau_i^x$. Overall, while it is safe to assume that the electron temperature is a flux function, our simplified estimates here indicate that ion and impurity temperature could potentially vary poloidally over a substantial part of the pedestal.

It is interesting to address now the question what the radial shifts between HFS and LFS E_r wells in Figs. 5 (a) and 6 (a) would imply for the electron density. Taking the dominant terms in the parallel electron momentum equation and assuming that T_e is a flux function, the Boltzmann relation for the electrons follows

$$n_e(\rho, \theta) = n_e(\rho, \theta_0) \cdot \exp\left(\frac{e[\Phi(\rho, \theta) - \Phi(\rho, \theta_0)]}{T_e}\right). \quad (11)$$

Here, Φ is the plasma potential and θ the poloidal angle. Poloidal variations in Φ thus directly relate to variations in n_e . To get an idea of the order of the electron density variations resulting from the E_r well shifts, we plot in Fig. 9 the LFS E_r profile for the H-mode case together with the plasma potential profile obtained from radially integrating E_r and setting $\Phi = 0$ at the innermost point. Also shown in dashed blue is the same Φ profile, shifted out by $\Delta\rho = 0.015$, corresponding to the radial shift between HFS and LFS E_r well when they are aligned based on the temperature profiles. Fig. 9 suggests that shifts of this order result in plasma potential asymmetries in the region of the E_r well of ≈ 200 V and, assuming $T_z \approx T_e$, of $e\Delta\Phi/T_e \approx 0.6$. In that case, it follows from Eq. (11) that in the pedestal region, the LFS electron density would exceed the HFS one by a factor ≈ 1.8 . For the I-mode case, a similar analysis gives $\Delta\Phi \approx 100$ V and $e\Delta\Phi/T_e \approx 0.2$, resulting in a density asymmetry factor of ≈ 1.2 .

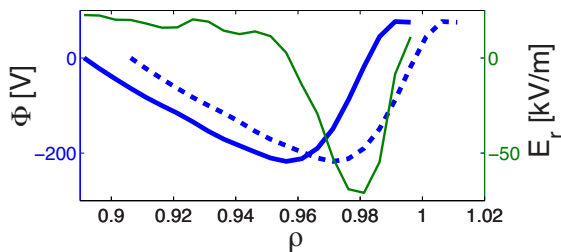


Figure 9. Shown is the LFS E_r profile from the EDA H-mode discharge in Fig. 3 (thin green), together with the plasma potential profile obtained from radially integrating E_r (thick blue). The dashed, blue curve shows again Φ , but shifted out by $\Delta\rho = 0.015$.

Next, we investigate implications from a simplified form of total parallel force balance. Adding up the parallel momentum equation for electrons and ions, treating the impurities as trace such that $n_e = n_i + Zn_z \approx n_i$, and defining the total pressure $p_{tot} = p_e + p_i$, we find

$$p_{tot}(\rho, \theta) - p_{tot}(\rho, \theta_0) = \int_{\theta_0}^{\theta} \left(\frac{-\mathbf{b} \cdot (\nabla \cdot \boldsymbol{\pi}_i)}{\mathbf{b} \cdot \nabla \theta} - \frac{m_i n_i}{\mathbf{b} \cdot \nabla \theta} \mathbf{b} \cdot (\mathbf{V}_i \cdot \nabla \mathbf{V}_i) \right) d\theta. \quad (12)$$

The integral over the poloidal angle θ includes terms due to ion viscosity and inertia. The corresponding terms for electrons have been neglected. We now write $T_e = T(\rho)$

and $T_i = T(\rho) + \delta T_i(\rho, \theta)$, such that with the above assumptions, we find

$$n_e = n_i = \frac{p_{tot}(\rho, \theta)}{2T(\rho) + \delta T_i(\rho, \theta)}. \quad (13)$$

Combining Eq. (13) with Eq. (11), we find the following expression for the HFS-LFS potential difference

$$\begin{aligned} \Phi^{LFS} - \Phi^{HFS} = & -\frac{T_e}{e} \log \left(1 + \frac{T_i^{LFS} - T_i^{HFS}}{2T + \delta T_i^{HFS}} \right) \\ & + \frac{T_e}{e} \log \left(\frac{p_{tot}^{LFS}}{p_{tot}^{HFS}} \right). \end{aligned} \quad (14)$$

We discuss here implications of Eq. (14) assuming that p_{tot} is a flux function and drops out. In this case, main ion temperature asymmetries can directly be related to potential asymmetries and, through Eq. (11), to electron density asymmetries. We note, however, that in particular the viscosity term in Eq. (12) is not expected to be negligible [12] and the goal of the following discussion is merely to gain some intuition.

We first assume that $T_i = T_z$. In this case, unless the shift between HFS and LFS E_r wells is very large, Figs. 5 (b) and 6 (b) show that we have $T_z^{LFS} - T_z^{HFS} > 0$ and hence also $T_i^{LFS} - T_i^{HFS} > 0$. From Eq. (14) and the assumption that $p_{tot}^{HFS} = p_{tot}^{LFS}$, it follows that $\Phi^{LFS} - \Phi^{HFS} < 0$. In this case, Fig. 9 suggests an *inward* shift of the HFS E_r well with respect to the LFS one, opposite to the shift obtained when the temperature profiles are aligned as in Figs. 5 (a) and 6 (a). It is interesting to note that a slight inward shift of the HFS E_r well with respect to the LFS one qualitatively agrees with potential asymmetries found by the code PERFECT [12] in the case of weak ion temperature gradients (see Fig. 1 and 2 of Ref. [46]). Figs. 5 (b) and 6 (b) show that when the HFS and LFS E_r wells are aligned, substantial poloidal asymmetries in T_z are observed as far in as $\rho \approx 0.97$. And these asymmetries become even larger when the HFS well is shifted in further. Especially for the H-mode case, from the time scale analysis in Fig. 8 (a), we do not expect significant HFS-LFS T_i asymmetries at $\rho \approx 0.97$. This seems to suggest that main ion temperature varies poloidally to a weaker extent than T_z and that HFS and LFS E_r wells approximately align.

6. Summary and conclusions

In this paper, we have presented inboard and outboard radial electric field measurements in the pedestal of H-mode and I-mode plasmas. The measurements are performed on Alcator C-Mod using a recently developed gas puff CXRS technique [18], used in previous studies to infer poloidal asymmetries of toroidal flow [19, 21] and impurity density [20, 22]. The measurements reveal a clear E_r well in the HFS and the LFS pedestal for both confinement regimes. While the E_r well has a radially symmetric structure in EDA H-mode, it is asymmetric in I-mode, with a stronger shear layer at the outer side of the well. In the radial impurity force balance used to deduce the radial electric field, this asymmetric structure is reflected in the poloidal flow term. The

poloidal flow is along the electron-diamagnetic drift direction over most of the pedestal. Near the separatrix, it is strongly sheared and changes to the ion-diamagnetic drift direction.

To study inboard-outboard variations of E_r and T_z , HFS measurements are mapped to the LFS along magnetic flux surfaces. This indicates that plasma potential and impurity temperature are not simultaneously flux functions in these pedestals. A number of uncertainties related with the measurement technique, including that of gas puff perturbations discussed in Appendix A, seem unable to explain these observations. At each measurement location, the relative alignment of E_r and T_z profiles is fixed. However, due to uncertainties in the magnetic equilibrium reconstruction, there is some freedom in the relative alignment between HFS and LFS profiles. This complicates a conclusion about which quantity varies poloidally to what extent. Aligning profiles assuming that T_z is a flux function results in an outward (towards larger minor radii) shift of the HFS E_r well with respect to the LFS one by ≈ 3 mm (H-mode) and ≈ 2.5 mm (I-mode), constituting a substantial fraction of the E_r well width. This alignment also implies that LFS electron density exceed that at the HFS by factors of up to ≈ 1.8 (H-mode) and ≈ 1.2 (I-mode). If we instead align HFS and LFS profiles based on the location of the E_r wells, we find that HFS and LFS poloidal impurity flow profiles also approximately align and are even identical within error bars in I-mode. The values of T_z are then higher at the LFS than at the HFS by factors of up to ≈ 1.7 in the pedestal. A simplified form of total parallel force balance indicates that if main ion temperature is a flux function, the same is true for plasma potential. In this case, E_r wells approximately align and we find that LFS impurity temperature substantially exceeds the HFS one. A comparison of radial and parallel heat transport time scales indicates that, while electron temperature is a flux function, ballooning radial heat transport could be sufficient to cause some poloidal asymmetries in main ion temperature. If we assume that $T_i = T_z$ and neglect main ion viscosity and inertia, parallel force balance indicates that the HFS E_r well would shift *inwards* with respect to the LFS one. Such a shift would even further increase the HFS-LFS T_z asymmetry. Overall, the most likely explanation seems to be that main ion temperature varies poloidally to a weaker extent than T_z and that HFS and LFS E_r wells should be approximately aligned.

Finally, we note that there could be other reasons for temperature asymmetries than those discussed here when the pedestal width approaches the banana orbit width $\sqrt{\epsilon}\rho_i^\theta$. Indeed, on the LFS, hot ions from the pedestal top can reach further outwards on their banana orbit, while colder ones from the pedestal foot can reach inwards. This could cause temperature asymmetries for the less collisional main ions, which in turn could have a local effect on the impurity temperature. Also, magnetic drifts could still drive asymmetries for the more collisional impurities when ρ_z^θ/L_T or ρ_z^θ/L_{ne} becomes of order one [30]. More work is needed to quantify such effects for the plasmas investigated in this article.

Acknowledgments

We would like to thank the entire Alcator C-Mod team for making these experiments possible. This work was supported by US DOE Coop. Agreement No DE-FC02-99ER54512 and the Swiss National Science Foundation (SNSF).

Appendix A. Effect of the gas puff on local plasma parameters

The measurements presented in this work are obtained from GP-CXRS [18], which uses a gas puff to locally enhance charge exchange reactions. The difference between HFS and LFS impurity temperature when E_r profiles are aligned, Figs. 5 (b) and 6 (b), raises the question whether a local cooling of the gas puff could be responsible for this result. The deuterium puff is not expected to substantially cool the impurities directly. However, it could do so indirectly by cooling the main ions through charge exchange (an ion is replaced by a less energetic one) and by ionization (a relatively low energy ion is added). Below, we perform an estimate of the heat sink for the main ions caused by the gas puff and apply the time scale analysis of Sec. 5 to investigate its local effect. This suggests that energy losses due to the gas puff are not strong enough to cause substantial local perturbations in ion temperature. Already for a very weak local drop in T_i , parallel heat conduction is found to be large enough to make up for the energy sink. An unknown in this estimate is the parallel scale length of the assumed local perturbation of T_i along the magnetic field. However, it would have to be substantially larger than the distance along the magnetic field from HFS to LFS midplane to affect our conclusion. Besides this theoretical study, comparing GP-CXRS measurements of the LFS system between times where the gas puff intensity has dropped by a factor ≈ 5 gives an experimental indication that the gas puff indeed does not substantially affect the measurements.

To estimate the local cooling effect of the gas puff, we consider the following sources/sinks of main ion particles S_p , momentum \mathbf{S}_m , and energy S_E due to electron impact ionization and ion-neutral charge exchange

$$S_p = n_e n_n \langle \sigma^{ion} v \rangle \quad (\text{A.1})$$

$$\mathbf{S}_m = m_n \mathbf{V}_n S_p + \mathbf{S}_m^{CX} \quad (\text{A.2})$$

$$S_E = \frac{1}{2} m_n \langle v_n^2 \rangle S_p + S_E^{CX}, \quad (\text{A.3})$$

where

$$\begin{aligned} \mathbf{S}_m^{CX} &= \int f_i f_n \sigma_{CX} |\mathbf{v}_i - \mathbf{v}_n| (m_n \mathbf{v}_n - m_i \mathbf{v}_i) d^3 v_i d^3 v_n \\ S_E^{CX} &= \int f_i f_n \sigma_{CX} |\mathbf{v}_i - \mathbf{v}_n| \frac{1}{2} (m_n v_n^2 - m_i v_i^2) d^3 v_i d^3 v_n. \end{aligned}$$

Here, the newly introduced quantities are: neutral density and mass n_n and m_n , the electron impact ionization rate coefficient $\langle \sigma^{ion} v \rangle$, the $D^+ - D^0$ charge exchange cross-

section σ_{CX} , and the ion and neutral distribution functions f_i and f_n , taken to be drifting Maxwellians. With these definitions and since $m_n = m_i$, the term due to ionization and CX reactions on the right-hand side of the ion energy conservation equation, Eq. (3), takes the form

$$\begin{aligned} \frac{3}{2}n_i\frac{dT_i}{dt}\Big|_{ion,CX} &= \left(\frac{3}{2}(T_n - T_i) + \frac{1}{2}m_i(\mathbf{V}_n - \mathbf{V}_i)^2\right) S_p \\ &\quad - \mathbf{V}_i \cdot \mathbf{S}_m^{CX} + S_E^{CX}. \end{aligned} \quad (\text{A.4})$$

For the evaluation of Eq. (A.4), we use ionization and charge exchange cross section data from [47], and neglect the fluid drifts \mathbf{V}_n and \mathbf{V}_i . S_E^{CX} is evaluated by Monte Carlo integration. Gas puff modeling in [18] shows that due to charge exchange with the main ions, the neutral temperature T_n typically reaches 30% – 80% of T_i across the pedestal. In this range, S_E^{CX} varies nearly linearly with T_n/T_i and by a factor ≈ 3 . Setting $T_n/T_i = 0.5 = const.$ in the following is thus a reasonable approximation. The neutral density n_n is determined from the measured D_α radiance. Following [18], it is calculated as follows

$$n_n = \frac{4\pi I_{D_\alpha}}{PEC_{32}^{EXC} n_e \sqrt{\pi} W}, \quad (\text{A.5})$$

where I_{D_α} is the measured D_α radiance (in *photons/(sm²sr)*), PEC_{32}^{EXC} is the photon emission coefficient from ADAS [48], and W is the half-width of the gas puff. Simulations show that W depends on the distance into the plasma [18]. For our purpose, setting $W = 2 \text{ cm} = const.$ is appropriate. For the H-mode and I-mode discharge discussed in this paper, we then find that n_n/n_e decreases quickly into the plasma with values of $\approx 0.5\%$ around the separatrix. We find that the term in Eq. (A.4) due to charge exchange reactions exceed the one due to ionization by a factor that varies between 1.5 and 4 across the pedestal.

We perform now a time scale analysis similar to the one in Sec. 5 in order to estimate whether the gas puff causes substantial local perturbations of the ion temperature. The time scale τ_i^{cool} associated with the term in Eq. (A.4) is obtained using the definition in Eq. (4). To determine the time scale τ_i^\parallel necessary to homogenize the ion temperature along the magnetic field, we take into account that, in contrast to the case in Sec. 5, the gas puff effect is not axisymmetric. We consider a flux tube passing through the gas puff instead of the axisymmetric volume C_1 in Fig. 7, but otherwise repeat the same steps as in Sec. 5. This shows that Eqs. (8) and (9) remain valid as long as lB/B_θ is replaced by the puff width $2W$. The reason for this is that the extent of the heat source/sink along the magnetic field is now $2W$, while it is lB/B_θ in the axisymmetric case. An unknown here is the scale length L_\parallel of the temperature perturbation along the magnetic field, outside the source/sink region. As in the axisymmetric problem, Sec. 5, we take it to be the distance along the magnetic field between HFS and LFS and note that it would have to be much larger than that to affect our conclusion.

In Fig. A1, we plot τ_i^{cool} and τ_i^\parallel for the LFS puff for both the I-mode and H-mode case. We find that τ_i^\parallel is faster than τ_i^{cool} by factors of 50 and more. This suggests that the

gas puff does not lead to a significant local cooling of the plasma.

For discharges with a relatively small inner gap, gas puff neutral density near the sep-

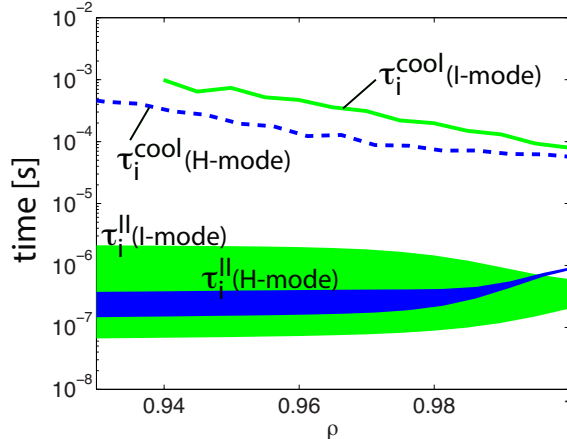


Figure A1. Comparison of the time scale at which a gas puff locally cools the main ions and the time scale at which a resulting temperature perturbation is homogenized along the magnetic field by parallel heat conduction. The shaded area for τ_i^{\parallel} is defined by the lower and upper bounds, Eqs. (8) and (9), where lB/B_θ was replaced by the puff width $2W$.

aratrix is sometimes found to be larger at the HFS than at the LFS, by factors reaching $\lesssim 8$. It is currently not understood why that is, as similar amounts of gas are injected at the HFS and at the LFS. However, there are discharges with larger inner gaps where HFS and LFS neutral densities agree within a factor two and these shots show a HFS-LFS mismatch in boron temperature and E_r similar to the cases reported in this work. We thus do not expect the gas puff to cause a significant local dip in temperature at the HFS either.

We note that understanding the effects of gas puffs on local and global plasma parameters is challenging (see [41] and references therein) and a systematic study by e.g. varying the gas puff rate for a number of reproducible discharges has not been performed. However, we note that from the available data, we typically do not see indications that the gas puff substantially perturbs the target plasma. For LFS puffs for example, the puff rate often varies relatively quickly over time, such that measurements for different instantaneous puff rates can be compared (on the HFS, due to a different setup of the gas line, the gas puffs strength varies much more slowly over time). An example is shown in Fig. A2 for an I-mode discharge. As the boron density stays fairly constant over time, Fig. A2 (d), the variation of the charge exchange brightness over time in Fig. A2 (a) directly represents the variation of the neutral density. As can be seen in Fig. A2 (b)-(e), despite a drop in the neutral density of about a factor of 5 between the two time windows highlighted in (a), the measured parameters are very similar.

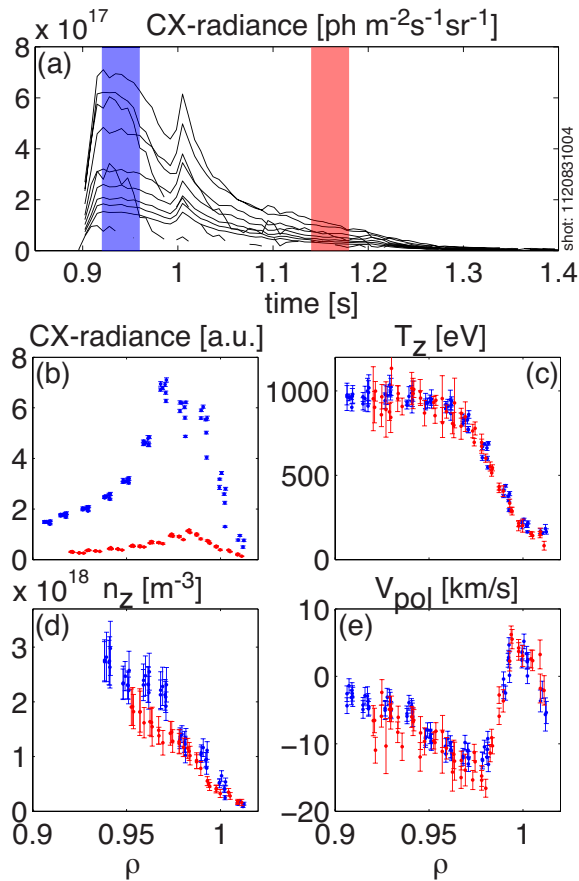


Figure A2. (a): Temporal variation of the CX brightness for the different views of the LFS poloidal system. (b)-(e): Different quantities measured with GP-CXRS for the two time windows highlighted in (a).

- [1] F. Wagner, G. Becker, K. Behringer, D. Campbell, A. Eberhagen, W. Engelhardt, G. Fussmann, O. Gehre, J. Gernhardt, G. V. Gierke, G. Haas, M. Huang, F. Karger, M. Keilhacker, O. Klüber, M. Kornherr, K. Lackner, G. Lisitano, G. G. Lister, H. M. Mayer, D. Meisel, E. R. Müller, H. Murmann, H. Niedermeyer, W. Poschenrieder, H. Rapp, H. Röhr, F. Schneider, G. Siller, E. Speth, A. Stähler, K. H. Steuer, G. Venus, O. Vollmer, and Z. Yü. *Phys. Rev. Lett.*, 49:1408–1412, 1982.
- [2] R. J. Groebner and T. H. Osborne. *Phys. Plasmas*, 5:1800–1806, 1998.
- [3] J. W. Hughes, D. A. Mossessian, A. E. Hubbard, B. LaBombard, and E. S. Marmor. *Phys. Plasmas*, 9:3019–3030, 2002.
- [4] E. J. Doyle, W. A. Houlberg, Y. Kamada, V. Mukhovatov, T. H. Osborne, A. Polevoi, G. Bateman, J. W. Connor, J. G. Cordey, T. Fujita, X. Garbet, T. S. Hahm, L. D. Horton, A. E. Hubbard, F. Imbeaux, F. Jenko, J. E. Kinsey, Y. Kishimoto, J. Li, T. C. Luce, Y. Martin, M. Ossipenko, V. Parail, A. Peeters, T. L. Rhodes, J. E. Rice, C. M. Roach, V. Rozhansky, F. Ryter, G. Saibene, R. Sartori, A. C. C. Sips, J. A. Snipes, M. Sugihara, E. J. Synakowski, H. Takenaga, T. Takizuka, K. Thomsen, M. R. Wade, H. R. Wilson, ITPA Transport Physics Topical Group, I. Confinement Database, Modelling Topical Group, I. Pedestal, and Edge Topical Group. *Nucl. Fusion*, 47:18, 2007.
- [5] A. Loarte et al. Progress in the ITER Physics Basis Chapter 4: Power and particle control. *Nucl. Fusion*, 47:S203, 2007.
- [6] D. G. Whyte, A. E. Hubbard, J. W. Hughes, B. Lipschultz, J. E. Rice, E. S. Marmor, M. Greenwald,

- I. Cziegler, A. Dominguez, T. Golfopoulos, N. Howard, L. Lin, R. M. McDermott, M. Porkolab, M. L. Reinke, J. Terry, N. Tsujii, S. Wolfe, S. Wukitch, Y. Lin, and Alcator C-Mod Team. *Nucl. Fusion*, 50:105005, 2010.
- [7] M. Greenwald, R. Boivin, P. Bonoli, R. Budny, C. Fiore, J. Goetz, R. Granetz, A. Hubbard, I. Hutchinson, J. Irby, B. Labombard, Y. Lin, B. Lipschultz, E. Marmor, A. Mazurenko, D. Mossessian, T. Sunm Pedersen, C. S. Pitcher, M. Porkolab, J. Rice, W. Rowan, J. Snipes, G. Schilling, Y. Takase, J. Terry, S. Wolfe, J. Weaver, B. Welch, and S. Wukitch. *Phys. Plasmas*, 6:1943–1949, 1999.
- [8] K. H. Burrell, T. H. Osborne, P. B. Snyder, W. P. West, M. E. Fenstermacher, R. J. Groebner, P. Gohil, A. W. Leonard, and W. M. Solomon. *Nucl. Fusion*, 49:085024, 2009.
- [9] K. H. Burrell. *Phys. Plasmas*, 6:4418–4435, 1999.
- [10] P. W. Terry. *Rev. Mod. Phys.*, 72:109–165, 2000.
- [11] G. Kagan and P. J. Catto. *Plasma Phys. Control. Fusion*, 52:055004, 2010.
- [12] M. Landreman and D. R. Ernst. *Plasma Phys. Control. Fusion*, 54:115006, 2012.
- [13] T. Fülöp and P. Helander. *Phys. Plasmas*, 8:3305–3313, 2001.
- [14] D. Battaglia et al. *Bull. Am. Phys. Soc.*, 58:16, 2013.
- [15] I. H. Hutchinson, R. Boivin, F. Bombarda, P. Bonoli, S. Fairfax, C. Fiore, J. Goetz, S. Golovato, R. Granetz, M. Greenwald, S. Horne, A. Hubbard, J. Irby, B. Labombard, B. Lipschultz, and et al. *Phys. Plasmas*, 1:1511–1518, 1994.
- [16] E. Marmor and Alcator C-Mod Group. *Fusion Sci. Technol.*, 51:261, 2007.
- [17] M. Greenwald, A. Bader, S. Baek, H. Barnard, W. Beck, W. Bergerson, I. Bespamyatnov, M. Bitter, P. Bonoli, M. Brookman, et al. *Nucl. Fusion*, 53(10):104004, 2013.
- [18] R. M. Churchill, C. Theiler, B. Lipschultz, R. Dux, T. Pütterich, E. Viezzer, and the Alcator C-Mod and ASDEX Upgrade Teams. *Rev. Sci. Instrum.*, 84:093505, 2013.
- [19] K. D. Marr, B. Lipschultz, P. J. Catto, R. M. McDermott, M. L. Reinke, and A. N. Simakov. *Plasma Phys. Control. Fusion*, 52:055010, 2010.
- [20] R. M. Churchill, B. Lipschultz, C. Theiler, and the Alcator C-Mod Team. *Nucl. Fusion*, 53:122002, 2013.
- [21] T. Pütterich, E. Viezzer, R. Dux, R. M. McDermott, and the ASDEX Upgrade Team. *Nucl. Fusion*, 52:083013, 2012.
- [22] E. Viezzer, T. Pütterich, E. Fable, A. Bergmann, R. Dux, R. M. McDermott, R. M. Churchill, M. G. Dunne, and the ASDEX Upgrade Team. *Plasma Phys. Control. Fusion*, 55(12):124037, 2013.
- [23] F. Ryter, W. Suttrop, B. Brüsehaber, M. Kaufmann, V. Mertens, H. Murmann, A. G. Peeters, J. Stober, J. Schweinzer, H. Zohm, and ASDEX Upgrade Team. *Plasma Phys. Control. Fusion*, 40:725–729, 1998.
- [24] R. M. McDermott, B. Lipschultz, J. W. Hughes, P. J. Catto, A. E. Hubbard, I. H. Hutchinson, R. S. Granetz, M. Greenwald, B. Labombard, K. Marr, M. L. Reinke, J. E. Rice, D. Whyte, and Alcator C-Mod Team. *Phys. Plasmas*, 16:056103, 2009.
- [25] A. E. Hubbard, D. G. Whyte, R. M. Churchill, I. Cziegler, A. Dominguez, T. Golfopoulos, J. W. Hughes, J. E. Rice, I. Bespamyatnov, M. J. Greenwald, N. Howard, B. Lipschultz, E. S. Marmor, M. L. Reinke, W. L. Rowan, and J. L. Terry. *Phys. Plasmas*, 18:056115, 2011.
- [26] A. E. Hubbard, D. G. Whyte, R. M. Churchill, A. Dominguez, J. W. Hughes, Y. Ma, E. S. Marmor, Y. Lin, M. L. Reinke, and A. E. White. *Nucl. Fusion*, 52(11):114009, 2012.
- [27] I. Cziegler, P. H. Diamond, N. Fedorczak, P. Manz, G. R. Tynan, M. Xu, R. M. Churchill, A. E. Hubbard, B. Lipschultz, J. M. Sierchio, J. L. Terry, and C. Theiler. *Phys. Plasmas*, 20:055904, 2013.
- [28] A. E. White, P. Phillips, D. G. Whyte, A. E. Hubbard, C. Sung, J. W. Hughes, A. Dominguez, J. Terry, and I. Cziegler. *Nucl. Fusion*, 51(11):113005, 2011.
- [29] J. R. Walk et al. ELM Suppression and Pedestal Structure in I-Mode Plasmas. *Phys. Plasmas*, *accepted*, 2014.

- [30] P. Helander and D. J. Sigmar. *Collisional Transport in Magnetized Plasmas: Cambridge University Press*. 2005.
- [31] N. P. Basse et al. *Fusion Sci. Technol.*, 51:476, 2007.
- [32] Y. B. Kim, P. H. Diamond, and R. J. Groebner. *Phys. Fluids B*, 3:2050–2060, 1991.
- [33] S. P. Hirshman and D. J. Sigmar. *Nucl. Fusion*, 21:1079, 1981.
- [34] R. J. Fonck, D. S. Darrow, and K. P. Jaehnig. *Phys. Rev. A*, 29:3288–3309, 1984.
- [35] R. C. Isler. *Plasma Phys. Control. Fusion*, 36:171–208, 1994.
- [36] R. E. Bell, R. Andre, S. M. Kaye, R. A. Kolesnikov, B. P. Leblanc, G. Rewoldt, W. X. Wang, and S. A. Sabbagh. *Phys. Plasmas*, 17(8):082507, 2010.
- [37] T. Pütterich, E. Wolfrum, R. Dux, and C. F. Maggi. *Phys. Rev. Lett.*, 102:025001, 2009.
- [38] J. E. Rice, J. W. Hughes, P. H. Diamond, Y. Kosuga, Y. A. Podpaly, M. L. Reinke, M. J. Greenwald, Ö. D. Gürçan, T. S. Hahm, A. E. Hubbard, E. S. Marmor, C. J. McDevitt, and D. G. Whyte. *Phys. Rev. Lett.*, 106(21):215001, 2011.
- [39] L. Lao, H. St John, R. Stambaugh, A. Kellman, and W. Pfeiffer. *Nucl. Fusion*, 25:1611, 1985.
- [40] B. LaBombard et al. New insights on boundary plasma turbulence and the Quasi-Coherent Mode in Alcator C-Mod using a Mirror Langmuir Probe. *Phys. Plasmas*, *accepted*, 2014.
- [41] S. Zweben et al. "Effect of a deuterium gas puff on the edge plasma in NSTX", submitted to *Plasma Phys. Control. Fusion*. 2014.
- [42] D. Brunner, B. LaBombard, R. M. Churchill, J. Hughes, B. Lipschultz, R. Ochoukov, T. D. Rognlien, C. Theiler, J. Walk, M. V. Umansky, and D. Whyte. *Plasma Phys. Control. Fusion*, 55(9):095010, 2013.
- [43] F. I. Parra and P. J. Catto. *Plasma Phys. Control. Fusion*, 52(4):045004, 2010.
- [44] J. D. Callen, R. J. Groebner, T. H. Osborne, J. M. Canik, L. W. Owen., A. Y. Pankin, T. Rafiq, T. D. Rognlien, and W. M. Stacey. *Nucl. Fusion*, 50(6):064004, 2010.
- [45] L. D. Horton, A. V. Chankin, Y. P. Chen, G. D. Conway, D. P. Coster, T. Eich, E. Kaveeva, C. Konz, B. Kurzan, J. Neuhauser, I. Nunes, M. Reich, V. Rozhansky, S. Saarelma, J. Schirmer, J. Schweinzer, S. Voskoboynikov, E. Wolfrum, and ASDEX Upgrade Team. *Nucl. Fusion*, 45:856–862, 2005.
- [46] I. Pusztai, M. Landreman, A. Mollén, Y. O. Kazakov, and T. Fülöp. *Contrib. Plasma Phys.*, *submitted*, 2013.
- [47] R. K. Janev, W. D. Langer, and K. Evans. *Elementary processes in Hydrogen-Helium plasmas - Cross sections and reaction rate coefficients*. 1987.
- [48] H. Summers. *ADAS User Manual: Technical Report (University of Strathclyde)*. 2004.